

Collision-Free Robot Navigation in Crowded Environments using Learning based Convex Model Predictive Control

Zhuanglei Wen, Mingze Dong, and Xiai Chen

Abstract—The advent of deep reinforcement learning (DRL) has significantly expanded the application range for autonomous robots. However, safe navigation in crowded and complex environments remains a persistent challenge. This study proposes a robot navigation strategy that utilizes DRL, conceptualizing the observation as the convex static obstacle-free region, a departure from traditional reliance on raw sensor inputs. The novelty of this work is threefold: (1) Formulating an action space that includes both short-term and long-term reference points, based on the robot's kinematic limits and the convex region computed from 2D LiDAR sensor data. (2) Exploring a hybrid solution that combines DRL with Model Predictive Control (MPC). (3) Designing a customized state space and reward function based on the static obstacle-free region, reference points, and the trajectory optimized by MPC. The effectiveness of these improvements has been confirmed through experimental results, demonstrating improved navigation performance in crowded and complex environments.

I. INTRODUCTION

Robot navigation in densely populated environments is still a challenge that has drawn significant attention from the global research community. This interest is heightened by the integration of advanced learning methodologies. The unpredictable dynamics of these environments necessitate a robust and efficient autonomous navigation strategy. Recent advances in machine learning and deep reinforcement learning (DRL) have propelled the exploration of neural networks for navigation in these challenging settings [1].

Traditional DRL-based navigation methods, which rely on training robots in simulated environment using simulated sensory inputs, often face real-world limitations due to discrepancies between simulation and reality, particularly with regard to noise and friction [2]. A significant challenge is the dependency on neural networks to issue action commands, a factor that can diminish performance when shifting from simulated environments to actual ones [3]. To address this challenge, researchers, including Gao et al. [4], have introduced innovative strategies. One effective approach involves separating the control mechanism from the neural network and employing control methodologies that are viable in real-world settings.

Inspired by these advancements, our study employs Model Predictive Control (MPC), valued for its ability to enforce hard constraints, ensuring control commands stay within predefined limits [5]. Consequently, we define the network

output as a series of reference points for MPC's reference trajectory. Furthermore, we utilize the convex static obstacle-free region derived from LiDAR point clouds as the constraint space. This strategy confines the MPC-optimized trajectory strictly within the convex region, thereby ensuring navigation that is both kinematically feasible and secure.

The principal contributions of this study are as follows:

- Designing the action and action space based on the convex static obstacle-free region derived from LiDAR data. To facilitate both short-term dynamic obstacle avoidance and long-term navigation, we characterize the action as the reference trajectory composed of reference points at specific time intervals. The action space is defined as the intersection of the convex region with the robot's motion limits, from which we sample static safe reference trajectory. Subsequently, MPC is employed to track the reference trajectory, incorporating the convex region constraint within the MPC formulation to ensure the generation of safe and reliable control commands. Furthermore, we develop customized state space and reward function based on the convex region, reference points, and MPC-optimized trajectory.
- Implementing a seven stage curriculum training strategy, tested through a series of detailed experiments. These included ablation studies that analyze effects of various action space designs and reward function configurations on navigation performance. Furthermore, a comparative evaluation against the Timed Elastic Band (TEB) method highlighted our training approach's superior performance.
- We have made our work open source by sharing both the implementation and benchmark data in a code repository accessible at https://github.com/sunnyhello369/flat_ped_sim.git.

II. RELATED WORK

Traditional navigation approaches for robots in crowded spaces, such as the velocity-based, force-based, and potential field methods [6], face challenges due to their reliance on simplistic assumptions about pedestrian dynamics. The Social Force Model (SFM) [7], along with techniques like Reciprocal Velocity Obstacles (RVO) [8] and ORCA [9], provide foundational frameworks for predicting pedestrian movements, yet they may not fully capture the unpredictability of real-world environments [10].

Chen et al. [11] have advanced the field by introducing an interactive Model Predictive Control (iMPC) framework that utilizes the iORCA model for enhanced prediction of

*Corresponding author: Mingze Dong

All authors are with the College of Mechanical and Electrical Engineering, China Jiliang University, Hangzhou 310018, Zhejiang, China
1801400116@cjlu.edu.cn

pedestrian movements, thereby improving robot navigation in crowded environments.

DRL methods are also applied for crowd navigation. Yao et al. [12] developed an end-to-end DRL network that, by distinguishing between obstacles and pedestrians and utilizing sensor data along with pedestrian maps, significantly enhances robotic navigation capability. On a related front, Wang et al. [13] crafted a hierarchical network of gated-recurrent-unit (GRU) for environment modeling to predict dynamic changes, which focuses on dynamic environment representation, adaptive perception mechanism, and adaptive reward function for collision-free motion planning policy.

In parallel, hybrid methods have also seen novel applications. Gao et al. [4] developed a method, encoding vehicle and predicted trajectories into binary image as the state of DRL framework. Action is defined as the vehicle's future positions in polar coordinates. They applied convex optimization to these discrete reference points, transforming them into a reachable trajectory for the vehicle to follow. This method decouples control from other processes, with DRL concentrating on suggesting reference positions and convex optimization ensuring the trajectory's practicality for vehicle implementation.

Linh et al. [14] have explored various planning methods, including traditional MPC, TEB, and DRL-based end-to-end navigation strategies. They designed a policy network as a navigation method selector, choosing the appropriate navigation strategy based on static and dynamic environmental information. Brito et al. [3] have proposed a DRL-based decision-planning method that recommends target positions for the MPC planner, facilitating navigation that considers interactions with other agents.

Our navigation strategy is similar to that of Gao et al. [4], where the action is defined as a sequence of future positions for the robot. However, to achieve better navigation performance and smoother motion trajectories in dynamic, crowded settings, our method employs a state observation based on the convex static obstacle-free region calculated from 2D LiDAR data. Furthermore, we incorporate the convex region into the design of the action-state space, the reward function, and our MPC framework used for tracking the reference trajectory.

III. METHOD

A. Problem Definition

We model our problem using a Partially Observable Markov Decision Process (POMDP), which is well-suited for environments with inherent uncertainties and dynamic conditions. Our POMDP model, $M = (S, A, T, R, \gamma)$, includes: state space S , action space A , state transition function T , reward function R , and discount factor $\gamma \in [0, 1)$. At time t , the action of the agent, a_t , consists of the short-term and long-term reference points, Q_t^s and Q_t^l , is formulated in Section III-C and the reward r_t detailed in Section III-F. The state of the agent, s_t , is defined in Section III-E.

B. Agent Dynamics

To facilitate computation in planning and control, the omni-directional mobile robot is simplified to a point mass. This simplification turns the robot's kinematics into a 2D third-order integral model. The model's state, $x = [p_x, p_y, v_x, v_y, a_x, a_y]^T$, captures the position, velocity, and acceleration, while the control input, $u = [j_x, j_y]^T$, denotes the jerk.

The state evolution of the system can be expressed as:

$$\begin{aligned} \dot{p}_x &= v_x & \dot{p}_y &= v_y \\ \dot{v}_x &= a_x & \dot{v}_y &= a_y \\ \dot{a}_x &= j_x & \dot{a}_y &= j_y \end{aligned} \quad (1)$$

C. Action Space Design Based on Convex Region

The convex static obstacle-free region is generated by the algorithm proposed by Zhong et al. [15], which can efficiently create reliable convex spaces among obstacles of any shape from LiDAR point cloud data.

To navigate around dynamic obstacles effectively, our action is designed as a sequence of reference points at specific time intervals. To reduce training complexity, this sequence is simplified to two points: one representing the robot's reference position after a control cycle (t_c) and the other after an MPC prediction horizon (T), corresponding to short-term and long-term reference points, respectively. The path from the robot's current position to these points forms the reference trajectory for MPC tracking.

In the design of the action space, we firstly ensure that the sampling of reference points is confined within the convex region. Then, centering on the robot's current position O and considering its kinematic limits, we define two circular areas. These circles, intersected with the convex region, constitute our short-term and long-term action spaces, as illustrated by the red areas in Fig. 1 and 2. The policy network is designed to output two pairs of two-dimensional data, which, after sigmoid activation, yield $\hat{a}_t = \{(\alpha_t^s, \beta_t^s), (\alpha_t^l, \beta_t^l) | \alpha_t, \beta_t \in (0, 1)\}$.

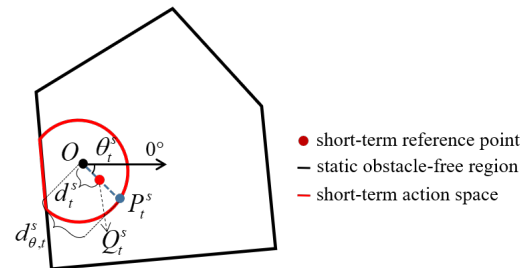


Fig. 1: Schematic of Short-Term Reference Point Formulation

The short-term reference point's coordinate, Q_t^s , is calculated as Equation 2, with Fig. 1 illustrating this process. A ray at angle θ_t^s intersects with the short-term action space at P_t^s . We determine P_t^s by calculating the polar angles of the convex's vertices and finding which edge the angle θ_t^s falls within. This intersection, is solved by combining

the ray and the edge equations, yields P_t^s in the LiDAR Cartesian system. Multiplying the distance from O to P_t^s , $d_{\theta,t}^s$, by the distance scaling factor β_t^s , we get the distance d_t^s , as formulated in Equation 2.

$$\begin{aligned}\theta_t^s &= \alpha_t^s \cdot 2\pi \\ d_t^s &= \beta_t^s \cdot d_{\theta,t}^s \\ Q_t^s &= (d_t^s \cdot \cos(\theta_t^s), d_t^s \cdot \sin(\theta_t^s))\end{aligned}\quad (2)$$

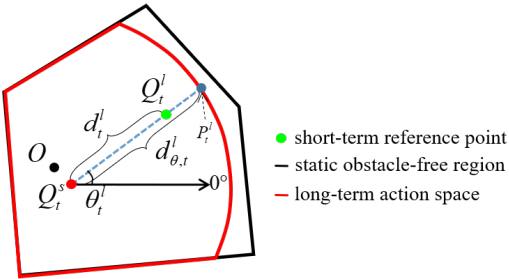


Fig. 2: Schematic of Long-Term Reference Point Formulation

The coordinate of the long-term reference point, Q_t^l , relative to O , is calculated as Equation 3, with Fig. 2 illustrating the process. We establish a new polar coordinate system centered at the short-term reference point Q_t^s . The long-term reference angle, θ_t^l , is calculated by adding a increment angle, $\alpha_t^l \cdot 2\pi$, to θ_t^s . A ray at angle θ_t^l intersects with the long-term action space at P_t^l . Following the procedure used for the short-term position, we can determine the coordinates of Q_t^l .

$$\begin{aligned}\theta_t^l &= \theta_t^s + \alpha_t^l \cdot 2\pi \\ d_t^l &= \beta_t^l \cdot d_{\theta,t}^l \\ Q_t^l &= Q_t^s + (d_t^l \cdot \cos(\theta_t^l), d_t^l \cdot \sin(\theta_t^l))\end{aligned}\quad (3)$$

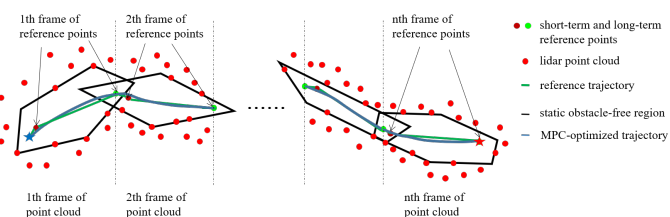


Fig. 3: Schematic of Iterative Trajectory Optimization within the Convex Region

To navigate safely in unknown environment, our method leverages real-time LiDAR data to generate the convex static obstacle-free region for local navigation. By ensuring the reference trajectory remains within the lasted convex region, collision with static obstacles can be avoided. The reference trajectory, connecting both long-term and short-term reference points, illustrated by the green solid line in Fig. 3. Subsequently, the MPC framework solves the local navigation problem by computing the optimal control inputs, thereby enabling the robot to adhere to the reference

trajectory. This process is iteratively repeated, ensuring the robot can follow updated trajectory and reach its target without colliding with obstacles.

D. Model Predictive Control Formulation

Let t_c represent the control period. If the MPC forecasts the system's state over N future control periods, the total prediction duration is $T = N \cdot t_c$. The initial state $x_{init} = [p_x^0, p_y^0, v_x^0, v_y^0, a_x^0, a_y^0]^T$ reflects the observed state at the start of the period.

Upon the discretization of the two-dimensional, third-order integral model governing robotic dynamics (referenced in Section III-B, Equation 1), the sequential relationship is obtained as $x_i = Fx_{i-1} + Gu_{i-1}$ for $i = \{1, \dots, N\}$. In this formulation, F signifies the matrix defining the discrete-time state transitions, while G delineates the matrix characterizing the discrete-time control inputs.

Using the method mentioned in Section III-C, we get a convex region from point cloud data, with its vertices $P_j^c, j = \{1, \dots, rnum_v\}$ arranged in clockwise direction. This region limits the MPC-optimized points to ensure safety by preventing collisions with static obstacles. This constraint is efficiently met by determining whether the trajectory point Q_i is inside the convex region through a streamlined vector method $\overrightarrow{Q_i P_j^c} \times \overrightarrow{Q_i P_{j+1}^c} \leq 0$.

During navigation, this vector method also is used to verify if the goal endpoint lies within the convex region. If so, this endpoint is directly used as the long-term reference point Q_t^l , which promotes early training by facilitating the acquisition of high-reward trajectories. And we also introduce a final state stop cost, $\cos t_{stop}$, into the MPC's cost function when the goal is within the convex region. This cost aims to minimize both the velocity $V_N = (v_x^N, v_y^N)$ and acceleration $A_N = (a_x^N, a_y^N)$ at the destination, ensuring a controlled and safe termination of movement. The final state stop cost $\cos t_{stop}$ is defined in Equation 4.

The short-term and long-term reference points are used to guide the positions of the first and last control period states predicted by the MPC. The cost function incorporates discrepancies between MPC-predicted points and reference points to ensure fidelity to the reference trajectory. Ultimately, the MPC formulation is approached as a quadratic programming problem, formulated in Equation 5, optimizing the control sequence $u_{0:N-1}^*$. The optimization produces a series of MPC-optimized points $Q_i^*, i = \{1, \dots, N\}$, forming the MPC-optimized trajectory, as depicted in Fig. 4.

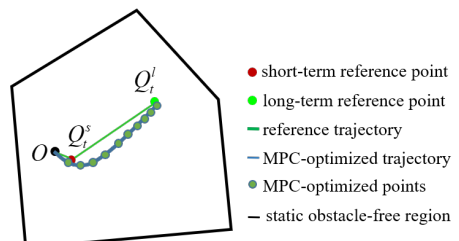


Fig. 4: Schematic of MPC Optimization Process

$$\cos t_{stop} = \begin{cases} w_{vend} \|V_N\|^2 \\ + w_{aend} \|A_N\|^2 & \text{if goal in convex} \\ 0 & \text{otherwise} \end{cases} \quad (4)$$

$$\begin{aligned} & \min_{u_{0:N-1}} w_{track} \left(\|Q_1 - Q_t^s\|^2 + \|Q_N - Q_t^l\|^2 \right) \\ & + w_{smooth} \sum_{k=0}^{N-1} \|u_k\|^2 + \cos t_{stop} \\ \text{s.t. } & x_0 = x_{init}, \\ & x_i = Fx_{i-1} + Gu_{i-1}, \\ & \overrightarrow{Q_i P_j^c} \times \overrightarrow{Q_i P_{j+1}^c} \leq 0, \\ & u_{i-1} \in \mathcal{U}, \bar{x}_i \in \mathcal{S}, \\ & \forall i \in \{1, \dots, N\}; \forall j = \{1, \dots, rnum_v - 1\}. \end{aligned} \quad (5)$$

E. Observation Space Formulation

At time t , the observation for the agent, o_t , as illustrated in Equation 6 and Figure 5, includes: the Euclidean distance d_t from robot to navigation goal, the velocity magnitude v_t , the angular deviation $d\theta_t$ between robot's velocity direction and the line to goal, the short-term and long-term reference points Q_{t-1}^s and Q_{t-1}^l from the previous frame's action, the MPC-optimized points Q_1^* and Q_N^* (defined in Section III-D), and the convex region $convex_t$.

$$o_t = (convex_t, d_t, v_t, d\theta_t, Q_{t-1}^s, Q_{t-1}^l, Q_1^*, Q_N^*) \quad (6)$$

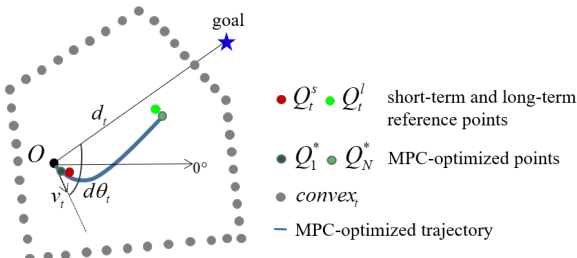


Fig. 5: Schematic of the Observation Vector

Due to the variability in shape of the convex static obstacle-free region ($convex_t$) derived from different point cloud data, the number of vertices in convex polygons is not constant. This poses a challenge for neural networks, which require input of fixed dimension. To address this issue, the vertex count of the computed convex region, num_v , is adjusted to match the predefined number $rnum_v$: vertices are added through interpolation if the count num_v is less than $rnum_v$, or reduced via sparsification if num_v exceeds $rnum_v$.

The agent can extract motion information about dynamic obstacles and its own historical trajectories from continuous frames implicitly. We define the agent's state as $s_t = (o_{t-2}, o_{t-1}, o_t)$, a concatenation of observations from three consecutive frames. This state representation, with its dimensionality set to $6rnum_v + 33$, optimizes the processing of

temporal and spatial information, enhancing the decision-making process.

F. Reward Function Formulation

The reward function plays a crucial role by setting the missions for agent. Agent's strategy is formulated based on the anticipation of future rewards, making reward function a critical mechanism for conveying tasks to the agent.

A positive reward, $r_{success}$, is awarded to the agent when its Euclidean distance to the navigation goal, d_t , falls below specified threshold, d_{th} , indicating successful arrival at the destination.

$$r_t^s = \begin{cases} r_{success} & \text{if } d_t < d_{th}, \\ 0 & \text{otherwise.} \end{cases} \quad (7)$$

Collision penalty r_t^o , derived from distance data $scan$ collected by LiDAR, is dynamically adjusted. The penalty decrease exponentially as the distance increases, controlled by a positive decay factor w_{obs} .

$$r_t^o = \begin{cases} r_{collision} & \text{if } \min(scan) \leq 0 \\ r_{obs} e^{-w_{obs} \min(scan)} & \text{if } \min(scan) \leq 2 \\ 0 & \text{otherwise} \end{cases} \quad (8)$$

To mitigate sparse reward, we incorporate potential-based reward shaping. A global path is computed at each episode using the Hybrid A* algorithm [16], based on robot's starting position, destination, kinematics, and global map. This path, used solely for reward calculation, informs the establishment of the Frenet [17] coordinate for tracking the robot's position (ς_t, l_t) , where ς_t is the longitudinal displacement and the lateral deviation l_t . The reward item r_t^a guides the agent towards the global path direction, while aiming to minimize lateral deviation l_t , a penalty r_t^l is introduced, as depicted in Equation 9 and Fig. 6.

$$\begin{aligned} r_t^a &= \begin{cases} 0 & \text{if } t = 1 \\ w_{approach}(\varsigma_t - \varsigma_{t-1}) & \text{otherwise} \end{cases} \\ r_t^l &= w_{close} l_t^2 \end{aligned} \quad (9)$$

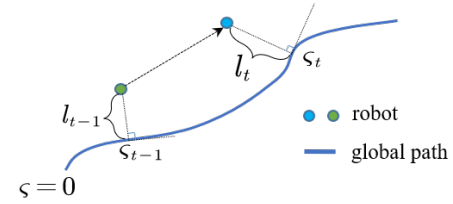


Fig. 6: Schematic of Global Path Based Potential Shaping Reward

In environment dense with dynamic obstacles, the optimal path diverges significantly from that in static settings, rendering potential shaping reward based on global path ineffective for accurate behavior assessment. To address this, we introduce a potential shaping reward r_t^{a2} , based on the Euclidean distance d_t between the robot and its destination.

$$r_t^{a2} = \begin{cases} 0 & \text{if } t = 1 \\ w_{approach2}(d_t - d_{t-1}) & \text{otherwise} \end{cases} \quad (10)$$

Short-term and long-term reference points, Q_t^s and Q_t^l , discussed in Section III-C, might not be practical to achieve. However, the MPC-optimized positions $Q_i^*, i = \{1, \dots, N\}$, outlined in Section III-D, comply with kinematic constraints and provide a more feasible reference. Thus, to penalize the error between reference points and MPC-optimized points, we introduce r_t^f , which encourages the generation of more reachable reference points.

$$r_t^f = w_{feasible}^s \|Q_t^s - Q_1^*\|^2 + w_{feasible}^l \|Q_t^l - Q_N^*\|^2 \quad (11)$$

Significant changes in reference points across frames can lead to discrepancies in both the length and direction of the MPC-optimized trajectory, demanding increased control efforts to counteract the impact of preceding frame. To address this, a penalty, r_t^c , on changes in reference points is introduced. This penalty can also facilitate rapid learning of smooth direction change during the initial training phase.

$$r_t^c = \begin{cases} 0 & \text{if } t = 1 \\ w_{change}^s \|Q_t^s - Q_{t-1}^s\|^2 \\ + w_{change}^l \|Q_t^l - Q_{t-1}^l\|^2 & \text{otherwise} \end{cases} \quad (12)$$

Ultimately, the fixed per-step penalty, denoted as r_t^e , is introduced.

The final reward function, denoted as r_t , is composed of above eight components. These components can be adjusted or selectively ignored during phases of training.

$$r_t = r_t^e + r_t^s + r_t^a + r_t^{a2} + r_t^l + r_t^o + r_t^c + r_t^f \quad (13)$$

G. Network Architecture

The convex static obstacle-free region efficiently removes redundant information from the raw LiDAR point cloud, including noise, duplicate points, and distant obstacles. This preprocessing step enables the adoption of a more streamlined network architecture for fitting policy and value functions, as depicted in Figure 7. Given that separate networks can yield better performance in practice [18], the policy and value network are updated independently, without sharing parameters.

IV. EXPERIMENTS

In this section, we introduce our training process along with the definition of seven Stages that vary in complexity (Table I). These stages are specifically designed for curriculum learning and subsequent evaluation. Following this, we evaluate our method in three parts:

(1) To demonstrate the advantages of our method in terms of action and state space design, we conduct an ablation study. This study compares our approach with four different DRL navigation methods constructed with various action and state spaces (Section IV-B).

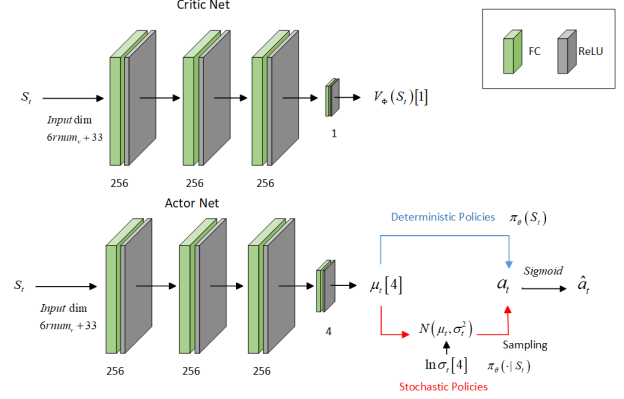


Fig. 7: Network Architecture: The value network V_ϕ and policy network π_θ are structured as four-layer fully connected networks. The policy network is augmented with a log standard deviation parameter ($\ln \sigma_t$) for each action dimension. This configuration primarily facilitates the generation of stochastic policies by allowing actions to be sampled from a Gaussian distribution, where σ_t , derived from $\ln \sigma_t$, modulates the balance between exploration and exploitation.

(2) To validate the effectiveness of our method in reward function design, we conduct another ablation study. This study compares our method against three other DRL navigation methods with different reward configurations (Section IV-C).

(3) To further analyze our method's advantages over non-DRL navigation methods in dynamic and crowded environments, we compare our method with the Timed Elastic Band (TEB) method in test scenarios (Section IV-D).

A. Training Procedure

Our method employs a multi-stage training strategy that progresses from simple to complex scenarios, rooted in the principles of curriculum learning, aiming to enhance the agent's learning efficiency by optimizing the sequence of experience acquisition. Initially, the agent learns basic navigation movements in an obstacle-free environment (Stage 1), and then it gradually encounters more static and dynamic obstacles.

1) *Stage Definition:* Table I displays the parameters of static and dynamic obstacles across seven Stages for staged training and subsequent evaluation. Static obstacles are randomly generated polygons with three or four sides, where the maximum area of these polygons does not exceed 2. The dynamic obstacles are circular in shape.

To assess the performance of the trained agent, we generate 1,000 test scenarios for each Stage, from 2 to 7, using random numbers not present in the training dataset to configure the simulator.

2) *Implementation Details:* Our work's leverages the Arena-Rosnav framework [19], developed within the ROS architecture, facilitating robust robotic navigation solutions. We also adopt the implementation of Proximal Policy Optimization (PPO) [20] from Elegant-RL [21], which offers

TABLE I: The Parameters of Static and Dynamic Obstacles in Seven Stages for Staged Training and Evaluation

Stage	Size (m)	Static Obstacles Count	Dynamic Obstacles Count	Dynamic Obstacle Radius Range (m)	Dynamic Obstacle Speed Range (m/s)
1	20×30	0	0	-	-
2	20×30	10	0	-	-
3	20×30	10	5	0.2-0.3	0.3
4	20×30	10	10	0.2-0.3	0.3
5	10×10	0	10	0.1-0.4	0.3-0.6
6	10×10	0	20	0.1-0.4	0.3-0.6
7	10×10	0	30	0.1-0.4	0.3-0.6

tools for network customization and training process monitoring. The simulation experiments are conducted on a high-performance PC equipped with an Intel Core i7-7700K CPU, an Nvidia RTX 2080Ti GPU, and 32GB of RAM.

B. Ablation Study on State and Action Space

To verify the effectiveness of the proposed method in terms of action and state space design, we conducted comparative experiments against four methods:

Design 1: Using the conventional end-to-end architecture where the observation o_t includes LiDAR data $scan'_t$. Action is defined as a set of two-dimensional velocities (v_x, v_y) , with the policy network's output layer using \tanh activation. The mapping from the policy network output (α_t, β_t) to (v_x, v_y) is detailed in (14).

$$o_t = (scan'_t, d_t, v_t, d\theta_t) \quad (14)$$

$$\hat{a}_t = \tanh(a_t) = \{(\alpha_t, \beta_t) | \alpha_t, \beta_t \in (-1, 1)\}$$

$$v_x = v_{min} + (v_{max} - v_{min}) \cdot \alpha_t$$

$$v_y = v_{min} + (v_{max} - v_{min}) \cdot \beta_t$$

Design 2: The state observation o_t updates to (15), incorporating the convex static obstacle-free region. The action, consisting of (v_x, v_y) , remains consistent with that of Design 1.

$$o_t = (convex_t, d_t, v_t, d\theta_t) \quad (15)$$

Design 3: The action is simplified to (Q_t^l) , focusing exclusively on long-term reference point. The calculation method of a single (Q_t^l) is similar to that of short-term reference point (Q_t^s) in Section III-C, except that single (Q_t^l) is sampled from the long-term action space. Additionally, Design 3 also streamlines the state observation as in (16) by removing terms related to Q_t^s .

$$o_t = (convex_t, d_t, v_t, d\theta_t, Q_{t-1}^l, Q_N^*) \quad (16)$$

Design 4: The observation o_t incorporates raw LiDAR data $scan'_t$, as in (17). The action is still (Q_t^l, Q_t^s) , but calculated within the intersection of the point cloud's coverage and the robot's kinematic limits. Given that $scan'_t$ is non-convex and

cannot be used as a constraint for convex optimization, the constraint that the optimized trajectory must be within the convex region is removed during the MPC calculation.

$$o_t = (scan'_t, d_t, v_t, d\theta_t, Q_{t-1}^s, Q_{t-1}^l, Q_1^*, Q_N^*) \quad (17)$$

After training from Stage 2 to 4, the performance of our method and Designs 1 to 4 in test scenarios is presented in Table II.

TABLE II: Ablation Study on action and state space designs: Comparative results of our method and Design 1 to 4 Across 1,000 test scenarios for each of the Stages from 2 to 4

Stage	Method	Success Rate	Time (s)	Distance (m)	Speed (m/s)
2	Design 1	76%	4.0	11.28	2.87
	Design 2	76%	4.0	11.11	2.8
	Design 3	90.3%	9.0	15.26	1.72
	Design 4	83%	5.0	11.66	2.23
	Ours	89.2%	5.5	12.19	2.18
3	Design 1	79.9%	4.0	11.37	2.9
	Design 2	79%	4.0	11.4	2.88
	Design 3	87.8%	8.8	15.42	1.77
	Design 4	83.5%	4.9	11.59	2.24
	Ours	89.1%	5.9	13.04	2.17
4	Design 1	80.9%	3.9	11.25	2.95
	Design 2	75.1%	3.8	10.78	2.89
	Design 3	84.5%	9.0	15.13	1.69
	Design 4	83.7%	4.8	11.19	2.2
	Ours	85.5%	5.8	12.51	2.1

In terms of action space design, Design 3 simplifies action to a single long-term reference point. Although Design 3 has an average navigation success rate of 87.53%, close to our method's 87.93%, Design 3's average navigation time is 3.2s longer and the average navigation distance is 2.69m longer than our method in the three Stages. On the other hand, Designs 1 and 2, which utilize continuous two-dimensional velocity for the action space, exhibit success rates lower by 9% and 11.23%, respectively, compared to our method.

In terms of state space design, compared with Design 1 and 4 that directly use raw LiDAR data as the observation, our method's average navigation success rate is 9% and 4.53% higher, respectively. The ablation study demonstrates the effectiveness of our method in the design of the action and state space.

C. Ablation Study on Reward Function

To assess the effectiveness of our reward function design, particularly the r_t^c and r_t^f items, as detailed in Section III-F, we conducted the ablation study with four different reward configurations and evaluated them across 1000 test scenarios from Stage 5 to 7. The results are presented in Table III.

Reward function, the configuration used in our method, incorporates all items.

$$r_{t1} = r_t^e + r_t^s + r_t^a + r_t^{a2} + r_t^l + r_t^o + r_t^c + r_t^f \quad (18)$$

Reward function r_{t2} is based on r_{t1} but excludes the reference points change penalty (r_t^c).

$$r_{t2} = r_t^e + r_t^s + r_t^a + r_t^{a2} + r_t^l + r_t^o + r_t^f \quad (19)$$

Reward function r_{t3} is based on r_{t1} but excludes the MPC-optimized points error penalty (r_t^f).

$$r_{t3} = r_t^e + r_t^s + r_t^a + r_t^{a2} + r_t^l + r_t^o + r_t^c \quad (20)$$

Reward function r_{t4} excludes both the r_t^c and the r_t^f from r_{t1} .

$$r_{t4} = r_t^e + r_t^s + r_t^a + r_t^{a2} + r_t^l + r_t^o \quad (21)$$

TABLE III: Ablation Study on Reward Function Designs: Comparative results of four reward functions across 1,000 test scenarios for each of the Stage from 5 to 7

Stage	Reward	Success Rate	Time (s)	Distance (m)	Speed (m/s)	Total Abs Acc
5	r_{t1}	87.1%	2.9	4.59	1.57	26475.46
	r_{t2}	87.8%	2.9	4.65	1.57	27600.56
	r_{t3}	84.8%	3.4	4.38	1.40	27781.34
	r_{t4}	86.7%	2.9	4.65	1.58	26460.66
6	r_{t1}	78.1%	2.9	4.12	1.42	19507.60
	r_{t2}	77.3%	2.8	4.10	1.43	20397.66
	r_{t3}	73.1%	3.4	3.85	1.25	21988.81
	r_{t4}	74.6%	3.0	4.35	1.46	19950.77
7	r_{t1}	68.5%	3.1	4.22	1.36	6348.57
	r_{t2}	69.9%	3.0	4.15	1.37	7218.53
	r_{t3}	67.1%	3.6	3.98	1.19	6080.69
	r_{t4}	65.3%	2.9	3.88	1.36	5668.30

In assessing how composite reward function affect the smoothness of motion, Total Absolute Acceleration (Total Abs Acc) serves as a critical metric. Total Abs Acc is the sum of agent's absolute acceleration ($a_i = \frac{|v_{i+1} - v_i|}{\Delta t}$, where $\Delta t=0.1$ s) taken across steps within successful episodes. A lower Total Abs Acc implies a smoother motion strategy, which is vital for safe and smooth navigation.

The ablation study clarifies the significance of the MPC-optimized points error penalty (r_t^f) for success rates, as seen in r_{t1} 's performance, with success rates of 87.1%, 78.1%, and 68.5% across stages. Exclusion of r_t^f in r_{t3} leads to decreased success rates (84.8%, 73.1%, 67.1%), emphasizing its critical role. Conversely, the reference points change penalty (r_t^c) slightly affects success rates but is significant for motion smoothness, where r_{t2} shows increased Total Abs Acc (27600.56 in Stage 5) compared to r_{t1} (26475.46 in Stage 5), indicating smoother navigation with r_t^c included. Overall, the results of the ablation study affirm the efficacy of our reward function design, highlighting the essential role of r_t^f for attaining higher success rate and the contribution of r_t^c to enhancing motion smoothness.

D. Evaluation

Following Stages 5-7's training in tight, dynamic crowded environments, both our method and TEB method are evaluated in 1,000 test scenarios for each Stage, with results detailed in Table IV.

Our method demonstrates a higher navigation success rate than the TEB method during all three Stages, outperforming TEB by 10.0%, 12.9%, and 10.7% respectively, which indicates our approach's superior obstacle avoidance capability in dense dynamic environments. Additionally, our method also

reduces navigation time by 1.5s, 1.1s, and 0.7s, and increases speed by 0.46m/s, 0.32m/s, and 0.29m/s, respectively. To analyze the navigation behavior differences between our method and TEB, scenarios from each stage are visualized in Figure 8. While TEB struggles with predicting the movement of dynamic obstacles, leading to potential collisions, our method proactively identifies and navigates through available gaps, allowing for more efficient obstacle avoidance.

TABLE IV: Comparative results of Our Method and TEB Method Across 1,000 test scenarios for each of the Stage from 5 to 7

Stage	Method	Success Rate	Time (s)	Distance (m)	Speed (m/s)
5	TEB	77.1%	4.4	4.64	1.11
	Ours	87.1%	2.9	4.59	1.57
6	TEB	65.2%	4.0	4.21	1.10
	Ours	78.1%	2.9	4.12	1.42
7	TEB	57.8%	3.8	3.87	1.07
	Ours	68.5%	3.1	4.22	1.36

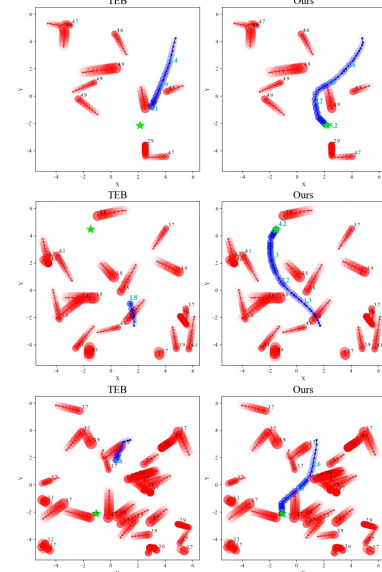


Fig. 8: Comparative Navigation Process: Our Method and TEB in Selected Test Scenarios from Stages 5, 6, 7. The three images, arranged from top to bottom, respectively depict the robot's navigation process during the test scenarios of Stages 5, 6, and 7. Light blue polygons for static obstacles, dark blue line marking robot trajectory, a green star for the goal, and cyan numbers indicate the time used by robot to move to this position, in seconds. Red lines with adjacent black numbers represent dynamic obstacles' paths and timing move to this position, respectively.

E. Qualitative Analysis

Figure 9 illustrates the navigation process, reflecting the iterative trajectory optimization procedure depicted in Figure 3. The robot updates the convex static obstacle-free region with the latest LiDAR data. Subsequently, long-term and

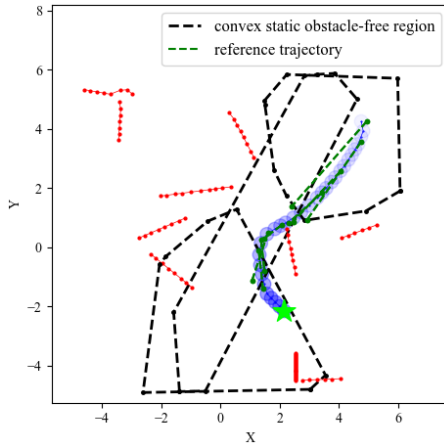


Fig. 9: Navigation Process of Our Method in a Test Scenario at Stage 5 for Qualitative Analysis: Fig. 9 and the first item of Fig. 8 depict the robot's navigation process during the same test scenario in Stage 5. However, for clearer observation, Fig. 9 omits the radius and timing of dynamic obstacles, as well as the robot's timing data. Instead, it introduces the convex static obstacle-free regions (indicated by black dashed lines) and a portion of reference trajectories (indicated by green dashed lines). The reference trajectory is formed by connecting long-term and short-term reference points, as detailed in Section III-C.

short-term reference points are sampled within this convex region to form the reference trajectory. The MPC then tracks this reference trajectory to solve the local navigation problem, until the goal endpoint is within the latest convex region and is directly adopted as the long-term reference point. The process ensures static safety by keeping both the reference trajectory and robot motion within the overlapping convex regions. Additionally, the frequent updating of reference points significantly enhances the dynamic safety, ensuring a robust response to environmental changes.

V. CONCLUSIONS

This paper introduces a DRL-based navigation framework, which consists of design of action and state spaces, reward function and network architecture. In terms of action space design, our method integrates lidar-generated convex static obstacle-free region to formulate action space that includes both short-term and long-term reference points. For the reward function, we devise a composite reward function enriched with intermediate rewards. We conduct training and experiments across seven Stages. The experimental results conclusively demonstrate that the proposed method significantly enhances robotic performance in both static and dynamic settings, notably excelling in dynamic and crowded environment.

REFERENCES

- [1] M. Everett, Y. F. Chen, and J. P. How, "Motion planning among dynamic, decision-making agents with deep reinforcement learning," in *2018 IEEE/RSJ International Conference on Intelligent Robots and Systems (IROS)*. IEEE, 2018, pp. 3052–3059.
- [2] T. Fan, P. Long, W. Liu, and J. Pan, "Distributed multi-robot collision avoidance via deep reinforcement learning for navigation in complex scenarios," *The International Journal of Robotics Research*, p. 856–892, Jun 2020. [Online]. Available: <http://dx.doi.org/10.1177/0278364920916531>
- [3] B. Brito, M. Everett, J. P. How, and J. Alonso-Mora, "Where to go next: Learning a subgoal recommendation policy for navigation in dynamic environments," *IEEE Robotics and Automation Letters*, vol. 6, no. 3, pp. 4616–4623, 2021.
- [4] F. Gao, P. Geng, J. Guo, Y. Liu, D. Guo, Y. Su, J. Zhou, X. Wei, J. Li, and X. Liu, "Apollor: A reinforcement learning platform for autonomous driving," *arXiv preprint arXiv:2201.12609*, 2022.
- [5] B. Paden, M. Cap, S. Z. Yong, D. Yershov, and E. Frazzoli, "A survey of motion planning and control techniques for self-driving urban vehicles," *IEEE Transactions on Intelligent Vehicles*, p. 33–55, Mar 2016. [Online]. Available: <http://dx.doi.org/10.1109/tiv.2016.2578706>
- [6] S. S. Samsani and M. S. Muhammad, "Socially compliant robot navigation in crowded environment by human behavior resemblance using deep reinforcement learning," *IEEE Robotics and Automation Letters*, vol. 6, no. 3, pp. 5223–5230, 2021.
- [7] D. Helbing and P. Molnar, "Social force model for pedestrian dynamics," *Physical review E*, vol. 51, no. 5, p. 4282, 1995.
- [8] J. Van den Berg, M. Lin, and D. Manocha, "Reciprocal velocity obstacles for real-time multi-agent navigation," in *2008 IEEE international conference on robotics and automation*. Ieee, 2008, pp. 1928–1935.
- [9] J. van den Berg, S. J. Guy, M. Lin, and D. Manocha, *Reciprocal n-Body Collision Avoidance*, Jan 2011, p. 3–19. [Online]. Available: http://dx.doi.org/10.1007/978-3-642-19457-3_1
- [10] S. S. Samsani and M. S. Muhammad, "Socially compliant robot navigation in crowded environment by human behavior resemblance using deep reinforcement learning," *IEEE Robotics and Automation Letters*, p. 5223–5230, Jul 2021. [Online]. Available: <http://dx.doi.org/10.1109/lra.2021.3071954>
- [11] Y. Chen, F. Zhao, and Y. Lou, "Interactive model predictive control for robot navigation in dense crowds," *IEEE Transactions on Systems, Man, and Cybernetics: Systems*, vol. 52, no. 4, pp. 2289–2301, 2021.
- [12] S. Yao, G. Chen, Q. Qiu, J. Ma, X. Chen, and J. Ji, "Crowd-aware robot navigation for pedestrians with multiple collision avoidance strategies via map-based deep reinforcement learning," in *2021 IEEE/RSJ International Conference on Intelligent Robots and Systems (IROS)*. IEEE, 2021, pp. 8144–8150.
- [13] S. Wang, R. Gao, R. Han, S. Chen, C. Li, and Q. Hao, "Adaptive environment modeling based reinforcement learning for collision avoidance in complex scenes," in *2022 IEEE/RSJ International Conference on Intelligent Robots and Systems (IROS)*, 2022, pp. 9011–9018.
- [14] K. Linh, J. Cox, T. Buiyan, J. Lambrecht *et al.*, "All-in-one: A drl-based control switch combining state-of-the-art navigation planners," in *2022 International Conference on Robotics and Automation (ICRA)*. IEEE, 2022, pp. 2861–2867.
- [15] X. Zhong, Y. Wu, D. Wang, Q. Wang, C. Xu, and F. Gao, "Generating large convex polytopes directly on point clouds," *arXiv preprint arXiv:2010.08744*, 2020.
- [16] D. Dolgov, S. Thrun, M. Montemerlo, and J. Diebel, "Practical search techniques in path planning for autonomous driving," *Ann Arbor*, vol. 1001, no. 48105, pp. 18–80, 2008.
- [17] M. Werling, J. Ziegler, S. Kammel, and S. Thrun, "Optimal trajectory generation for dynamic street scenarios in a frenet frame," in *2010 IEEE international conference on robotics and automation*. IEEE, 2010, pp. 987–993.
- [18] R. Raileanu and R. Fergus, "Decoupling value and policy for generalization in reinforcement learning," in *International Conference on Machine Learning*. PMLR, 2021, pp. 8787–8798.
- [19] L. Kästner, T. Buiyan, L. Jiao, T. A. Le, X. Zhao, Z. Shen, and J. Lambrecht, "Arena-rosnav: Towards deployment of deep-reinforcement-learning-based obstacle avoidance into conventional autonomous navigation systems," in *2021 IEEE/RSJ International Conference on Intelligent Robots and Systems (IROS)*. IEEE, pp. 6456–6463.
- [20] J. Schulman, F. Wolski, P. Dhariwal, A. Radford, and O. Klimov, "Proximal policy optimization algorithms," *arXiv: Learning, arXiv: Learning*, Jul 2017.
- [21] X.-Y. Liu, Z. Li, Z. Yang, J. Zheng, Z. Wang, A. Walid, J. Guo, and M. I. Jordan, "Elegantrl-podracer: Scalable and elastic library for cloud-native deep reinforcement learning," *NeurIPS, Workshop on Deep Reinforcement Learning*, 2021.